

# Antarctic Ice-Sheet variability across the Eocene-Oligocene boundary climate transition

**Authors:** Simone Galeotti<sup>1,\*</sup>, Robert DeConto<sup>2</sup>, Timothy Naish<sup>3,4</sup>, Paolo Stocchi<sup>5</sup>, Fabio Florindo<sup>6</sup>, Mark Pagani<sup>7</sup>, Peter Barrett<sup>3</sup>, Steven M. Bohaty<sup>8</sup>, Luca Lanci<sup>1</sup>, David Pollard<sup>9</sup>, Sonia Sandroni<sup>10</sup>, Franco Talarico<sup>10,11</sup>, James C. Zachos<sup>12</sup>

## Affiliations:

<sup>1</sup> Pure and Applied Sciences Department, Università degli Studi di Urbino ‘Carlo Bo’, Località Crocicchia, 61029 Urbino, Italy

<sup>2</sup>Department of Geosciences, University of Massachusetts, USA

<sup>3</sup>Antarctic Research Centre, Victoria University of Wellington, PO Box 600, Wellington, New Zealand

<sup>4</sup>GNS Science, PO Box 30368, Lower Hutt, New Zealand

<sup>5</sup>NIOZ Royal Netherlands Inst Sea Res, NL-1790 AB Den Burg, Texel, Netherlands

<sup>6</sup>Istituto Nazionale di Geofisica e Vulcanologia, via di Vigna Murata 605, 00143 Rome, Italy

<sup>7</sup>Department of Geology and Geophysics, Yale University, USA

<sup>8</sup>Ocean and Earth Science, University of Southampton, National Oceanography Centre, Southampton SO14 3ZH, United Kingdom

<sup>9</sup>Earth System Science Center, Pennsylvania State University, USA

<sup>10</sup>Museo Nazionale dell’Antartide, Università degli Studi di Siena, via del Laterino 8, 53100, Italy

<sup>11</sup>Dipartimento di Scienze fisiche, della Terra e dell’Ambiente, Università degli Studi di Siena, via del Laterino 8, 53100 Siena, Italy

<sup>12</sup>Earth Sciences Department, University of California, Santa Cruz. Santa Cruz, CA 95064, US

\*Correspondence to: simone.galeotti@uniurb.it.

**Abstract:** About 34 million years ago (Ma) Earth’s climate cooled and an ice sheet formed on Antarctica as atmospheric CO<sub>2</sub> fell below ~750 ppm. Sedimentary cycles from a drill core in western Ross Sea provide the first direct evidence of orbitally-controlled glacial cycles between 34–31 Ma. Initially, under atmospheric CO<sub>2</sub> levels  $\geq$  600 ppm, a smaller Antarctic Ice Sheet (AIS) restricted to the terrestrial continent was highly responsive to local insolation forcing. A more stable, continental-scale ice sheet, calving at the coastline, did not form until ~32.8 Ma coincident with the first time atmospheric CO<sub>2</sub> levels fell below ~600 ppm. Our results provide new insights into the potential of the AIS for threshold behavior, and its sensitivity to atmospheric CO<sub>2</sub> concentrations above present day levels.

**One Sentence Summary:** Antarctic Ice Sheet sensitivity to insolation forcing and vulnerability increases dramatically with atmospheric CO<sub>2</sub> concentration above ~600 ppm.

**Main Text:** The establishment of the Antarctic Ice Sheet (AIS) is associated with an ~+1.5%

increase in deep-water marine oxygen isotopic ( $\delta^{18}\text{O}$ ) values beginning at  $\sim 34$  Ma and peaking at  $\sim 33.6$  Ma (1-4). Detailed records of this transition reveal two positive  $\delta^{18}\text{O}$  steps separated by  $\sim 200$  kyr. The first primarily reflects a temperature decrease (5). The second has been interpreted as the onset of a prolonged interval of maximum ice extent (Earliest Oligocene Glacial Maximum or EOGM) between 33.6–33.2 Ma (3). Deep-water temperature cooled by 3–5°C (6) as a consequence of decreasing  $\text{CO}_2$  levels (7), while the volume of ice on Antarctica expanded to either near modern dimensions (6, 8) or as much as 25% larger than present day (9, 10). A  $\sim 70$  m sea-level fall is estimated from low-latitude shallow marine sequences (9, 11). Uncertainties in the magnitudes of these estimates in part reflect the limitations of geochemical proxy records used to deconvolve the relative contribution of ice volume and temperature at orbital resolution (12), as well as uncertainties inherent to the backstripping of continental margin sedimentary records (8). Ice sheet proximal marine geological records from the continental margin of Antarctica can improve our understanding of the AIS evolution by providing evidence of the direct response of shallow-marine sedimentary environments (e.g. water depth changes) to ice-sheet expansion and retreat.

The temporal pattern and extent of Late Eocene–Early Oligocene ( $\sim 34.1$  Ma to  $\sim 31$  Ma) Antarctic glacial advance and retreat is recorded in the well-dated CRP-3 drill core, a shallow-water glaciomarine sedimentary succession deposited in the Victoria Land Basin (Fig. 1), tens of kilometres seaward of the present-day East Antarctic Ice Sheet (EAIS) in the Western Ross Sea (13). Thirty-seven fluvial to shallow-marine (deltaic) sedimentary cycles occur in the lower 500 m of the drill core (330–780 m below sea-floor; mbsf) that record the advance and retreat of land-terminating glaciers delivering terrigenous sediment to an open wave-dominated coastline and are associated with  $<20$  m oscillations in relative sea-level (RSL) (14). These cycles, characterized as 'Type B' (Fig. 2; see also SOM), do not display evidence of ice contact from glacial overriding. In contrast, eleven glaciomarine sedimentary cycles bounded by glacial surfaces of erosion in the upper 300 m of the drillcore (0–300 mbsf) reflect oscillations of the seaward extent of a marine-terminating ice sheet onto the Ross Sea continental shelf and across the CRP-3 drill site associated with larger RSL fluctuations of  $>20$  m (14) (Type A cycles in Fig. 2; see also SOM). Temporal variations in lithofacies, grain-size, and clast abundance primarily reflect oscillations in depositional energy that were controlled by changes in water depth and/or glacial proximity (14, 15). Shallow marine sedimentary cycles analogous to those observed in the CRP-3 drillcore have been directly linked with orbitally driven climatic cycles in the AIS across the Oligocene-Miocene boundary at a nearby Ross Sea site (16). Accordingly, we apply a similar approach to directly compare the timing of proximal ice-volume changes during the Early Oligocene against high-resolution temperature and ice-volume proxy records derived from distal deep-sea sequences. Clast abundance (Fig. 2) reflects glacial proximity and has been shown in a previous study to be controlled by orbital forcing in conjunction with the deposition of Type B cycles in the lower part of CRP-3 (17). To similarly test for the role of orbital forcing within the laterally extensive glacial advances within the Type A cycle succession in the upper 300 m of the CRP-3 core, we apply a Singular Spectrum Analysis (SOM) to the clast abundance time series and a new record of luminance, which reflects changing proportions of clay and sand in sedimentary environments controlled by the proximity to the ice margin and by changes in water depth associated with RSL fluctuations (14). An independently derived age model for CRP-3, based on biochronologic calibration of a magnetic reversal stratigraphy (17), together with identification of the orbital components in these records enables a one-to-one correlation of sedimentary cycles to the highly-resolved, orbitally tuned  $\delta^{18}\text{O}$  record from the deep sea (3, 18)

(Fig. 2). A key age constraint in the CRP-3 record is the precisely dated transition ( $\pm 5$ -kyrs) at 31.1 Ma between magnetic polarity Chrons C12n/C12r at 12.5 mbsf (17) (Fig. S5).

Variation in facies and clast abundance within Type B shallow-marine sedimentary cycles have previously been interpreted to reflect periodic advance and retreat of land terminating alpine glaciers in the Transantarctic Mountains (15) in response to precession and obliquity forcing (17) (Fig. 2). This direct response to orbitally paced local insolation forcing indicates a highly dynamic AIS during the early icehouse phase of the EOGM<sup>6</sup>. The first sedimentary evidence of ice advance onto the Ross Sea continental shelf coincides with the deposition of unconformity bound, Type A sedimentary cycles beginning at 32.8 Ma, and marks an abrupt transition in AIS sensitivity to orbital forcing that was paced by longer-duration eccentricity cycles (Figs. 2, 3). This phase is also associated with climate cooling and increased physical weathering as evidenced by a change in clay mineralogy (19). Type A cycles (Fig. 2) have been interpreted to represent cyclic alternations in both grounding-line proximity and RSL change (14). According to the Glacial Isostatic Adjustment (GIA) theory and given the ice marginal position of the CRP-3 site, any proximal ice-thickness variation would have triggered crustal and geoidal deformations such that the resulting local RSL change would be opposite in sign to the eustatic trend and likely of larger amplitude (see SOM). However, sedimentological evidence implies that glacial maxima and minima locally coincide with times of minimum and maximum RSL, respectively, for both Type A or Type B cycles (14). This implies that the GIA-induced RSL rise that was caused by the expansion and grounding of the ice sheet at the CRP-3 site was counter-balanced by a strong RSL drop as a consequence of the forebulge uplift that was driven by synchronous EAIS thickening. Therefore, we argue that the appearance of marine grounded ice near the CRP-3 site was enhanced by flexural uplift of the crust as the Eastern Antarctic Ice Sheet expanded resulting in a RSL fall ( $> 40$  m) in phase with the hypothetical eustatic trend. Both petrological and apatite fission track evidence (20) suggests that diamictites deposited as part of 400 kyr sedimentary cycles spanning  $\sim 17$ – $157$  mbsf ( $\sim 32.0$ – $31.1$  Ma; Fig. 2), were derived both locally from the Mackay glacier and from the southern Transantarctic Mountains outlet glaciers during glacial overriding and downcutting. Flowlines that trend northwestward into McMurdo Sound from the Byrd, Skelton and Mulock glaciers is implied by model simulation of the early Oligocene glacial expansion (1, 10).

Based on our chronology and geological evidence for ice-grounding, a marine calving ice sheet first occurred in western Ross Embayment at  $\sim 32.8$  Ma, approximately one million years after the glacial maximum (Oi1) inferred by  $\delta^{18}\text{O}$  values from marine carbonate isotope records (18) (Figs. 2, 3). Oxygen isotope values paired with southern high-latitude Mg/Ca records (4) indicate that the AIS volume was slightly larger across Oi1a ( $\sim 32.8$  Ma) than across the EOGM.

Importantly, the Oi1a interval coincides with the  $\text{CO}_2$  minimum ( $\sim 600$  ppmv) at the end of a  $\sim 40\%$  decline beginning in the late Eocene (2, 7) (Fig. 3). Declining  $\text{CO}_2$  levels that culminate during Oi1a are fully consistent with model-derived  $\text{CO}_2$  thresholds for Antarctic glaciation (1). The Oi1a interval also corresponds to a long-term minimum in eccentricity and obliquity (21), similar to the orbital configuration favouring the onset of glaciation across Oi1 (Fig. 3), implying that an extended period of low seasonality with cooler summers contributed to these long period glacial maxima (21).

Therefore, we argue that in spite of ice expansion during the EOGM, the nascent AIS was strongly sensitive to orbitally paced, local insolation forcing until a threshold of  $\sim 600$  ppmv was crossed at 32.8 Ma (Fig. 3; Fig. S15), after which an expanded continental-scale ice sheet displayed progressively stronger orbital ice-sheet hysteresis, which is also suggested by models

(1, 22). Our observations from the CRP-3 record are also consistent with far-field ice volume proxies that indicate RSL changes of ~25 m in the time interval between 33.4-32.8 Ma (9, 11), equivalent to ~40% of present-day AIS volume. Whereas, after 32.8 Ma, a protracted period of RSL stability is observed in  $\delta^{18}\text{O}$  records, which corresponds with our proximal evidence for an AIS that is relatively insensitive to higher frequency orbital forcing (11) until ~29 Ma, when  $\text{CO}_2$  values increase to above 600 ppm (23) (see Fig. S16). Therefore, we view atmospheric  $\text{CO}_2$  concentration as the primary influence on overall climate state and variability of AIS volume, especially its sensitivity to orbital forcing, which implies a close linkage between carbon cycle dynamics and AIS evolution on both the long-period and short-period orbital time scales. Indeed, the amplification of the long-period eccentricity component – observed in the CRP-3 record at ~32 Ma – tracks the establishment of low-latitude  $\delta^{13}\text{C}$  variability with a 405-kyr periodicity (24).

The general orbital coherence and phasing between glacial cycles and marine  $\delta^{13}\text{C}$  records (Fig. 2) suggest that carbon cycle feedbacks contributed to  $\text{CO}_2$  changes and amplification of short- and long-period eccentricity-paced glacial-interglacial cycles in the Early Oligocene (25), similar to the climate-carbon cycle dynamics associated with Northern Hemisphere glacial cycles during the Pleistocene. Coupled global climate-ice sheet models predict that the AIS displays threshold behaviour in response to long-term trends in atmospheric  $\text{CO}_2$  levels (26). For example the stability threshold for marine-based sectors of the AIS has been shown to be ~400ppm, and between 300-400ppm marine ice sheets are highly dynamic in response to orbital forcing (27, 28). Data presented in this study imply that a  $\text{CO}_2$  threshold for a continental-scale Antarctic ice sheet occurred at ~600 ppm, and AIS sensitivity to insolation forcing and vulnerability to melt increases dramatically between 600-750ppm.

## References and Notes:

1. R. DeConto, D. Pollard, *Nature* **421**, 245 (2003).
2. P. N. Pearson, G. L. Foster, B. S. Wade, *Nature* **461**, 1110 (2009).
3. H. K. Coxall, P. A. Wilson, H. Palike, C. H. Lear, J. Backman, *Nature* **433**, 53 (2005).
4. S. M. Bohaty, M. L. Delaney, J. C. Zachos, *Earth Planet. Sci. Lett.* **317–318**, 251 (2012).
5. C. H. Lear, T. R. Bailey, P. N. Pearson, H. K. Coxall, Y. Rosenthal, *Geology* **36**, 251 (2008).
6. Z. Liu *et al.*, *Science* **323**, 1187 (2009).
7. M. Pagani, J. C. Zachos, K. H. Freeman, B. Tipple, S. Bohaty, *Science* **309**, 600 (2005).
8. K. G. Miller *et al.*, *Bulletin of the Geological Society of America* **120**, 34 (2008).
9. M. E. Katz *et al.*, *Nature Geoscience* **1**, 329 (2008).
10. D. S. Wilson, D. Pollard, R. M. DeConto, S. S. R. Jamieson, B. P. Luyendyk, *Geophysical Research Letters* **40**, 4305 (2013).
11. K. G. Miller *et al.*, *Science* **310**, 1293 (2005).
12. K. Billups, D. P. Schrag, *Earth Planet Sc Lett* **209**, 181 (2003).
13. F. Florindo, G. S. Wilson, A. P. Roberts, L. Sagnotti, K. L. Verosub, *Global and Planetary Change* **45**, 207 (2005).
14. C. R. Fielding, T. R. Naish, K. J. Woolfe, *Terra Antarctica* **8**, 217 (2001).
15. T. R. Naish *et al.*, *Terra Antarctica* **8**, 225 (2001).
16. T. R. Naish *et al.*, *Nature* **413**, 719 (2001).
17. S. Galeotti *et al.*, *Palaeogeogr. Palaeoclimatol. Palaeoecol.* **335**, 84 (2012).

18. H. K. Coxall, P. A. Wilson, *Paleoceanography* **26**, (Jun 11, 2011).
19. W. Ehrmann, M. Setti, L. Marinoni, *Palaeogeography, Palaeoclimatology, Palaeoecology* **229**, 187 (2005).
20. V. Olivetti, M. L. Balestrieri, F. Rossetti, F. M. Talarico, *Tectonophysics* **594**, 80 (May 24, 2013).
21. J. Laskar *et al.*, *Astronomy and Astrophysics* **428**, 261 (2004).
22. D. Pollard, R. M. DeConto, *Global and Planetary Change* **45**, 9 (2005).
23. Y. G. Zhang, M. Pagani, Z. H. Liu, S. M. Bohaty, R. DeConto, *Philos T R Soc A* **371**, (Oct 28, 2013).
24. H. Pälike *et al.*, *Science* **314**, 1895 (2006).
25. J. C. Zachos, L. R. Kump, *Global and Planetary Change* **47**, 51 (2005).
26. R. M. DeConto, D. Pollard, *Nature* **421**, 245 (2003).
27. M. O. Patterson *et al.*, *Nature Geoscience* **7**, 841 (2014).
28. G. L. Foster, E. J. Rohling, *PNAS* **110**, 1209 (2013).
29. D. S. Wilson, *Palaeogeogr. Palaeoclimatol. Palaeoecol.* **335–336**, 24 (//, 2012).
30. S. Sandroni, F. Talarico, *Terra Antarctica* **8**, 449 (2001).
31. C. R. S. Team, *Terra Antarctica* **7**, 1 (2000).
32. R. D. Powell *et al.*, *Terra Antarctica* **8**, 207 (2001).
33. G. B. Dunbar, T. R. Naish, P. J. Barrett, C. R. Fielding, R. D. Powell, *Palaeogeogr. Palaeoclimatol. Palaeoecol* **260**, 50 (2008).
34. S. A. Henrys *et al.*, *Antarctica: A Keystone in a Changing World-Online Proceedings for the Tenth International Symposium on Antarctic Earth Sciences*, 4 (2007).
35. C. R. Fielding, J. Whittaker, S. A. Henrys, T. J. Wilson, T. R. Naish, - **260**, (2008).
36. P. G. Fitzgerald, E. Stump, *J. Geophys. Res. Solid Earth* **102**, 2156 (1997).
37. P. J. Barrett, *Terra Antarctica* **8**, 245 (2001).
38. M. Ghil *et al.*, *Reviews of Geophysics* **40**, 3 (2002).
39. C. R. S. Team, *Terra Antarctica* **8**, 1 (2001).
40. M. R. Allen, L. A. Smith, *Journal of Climate* **9**, 3373 (Dec, 1996).
41. F. Florindo, G. S. Wilson, A. P. Roberts, L. Sagnotti, K. L. Verosub, *Terra Antarctica* **8**, 599 (2001).
42. G. Spada, P. Stocchi, *Computers and Geosciences* **33**, 538 (2007).
43. M. Rugenstein, P. Stocchi, A. von der Heydt, H. Dijkstra, H. Brinkhuis, *Global and Planetary Change* **118**, 16 (2014).
44. P. Stocchi *et al.*, *Nature Geoscience* **6**, 380 (2013).

**Acknowledgments:** This research is an outcome of a two-year project (PNRA 2004/4.09) partly funded by the Italian PNRA. Additional support was provided by the NSF under awards ANT-0424589, 1043018, and OCE-1202632), and NZ Ministry of Business Innovation and Employment contract C05X1001(TN). Data are available from <http://www.pangaea.de/>

**Fig. 1.** Location of the CRP-3 drillsite on the maximum topography of Antarctica at ~34 Ma (10, 29).

**Fig. 2.** (A) Deep-sea oxygen and carbon isotopic record from ODP Site 1218 (3, 18), and time series for (B) climatic precession, (C) obliquity and (D) eccentricity correlated with the (E, F, G) magnetostratigraphy, lithostratigraphy and sequence stratigraphy (13, 15), and (H) square root of

clast abundance (30) for the Late Eocene-Early Oligocene CRP-3 drill core. (G) Thirty-seven shallow-marine sedimentary cycles (sequences; Type B) occur in the lower 500 m of the core record, controlled by advances and retreats of land-terminating glaciers associated with <20 m sea-level oscillations. Eleven overlying glaciomarine sedimentary cycles (sequences; Type A), each bounded by glacial surfaces of erosion, occur in the upper 300 m of the CRP-3 core, and record oscillations in the extent of a more expansive marine-terminating ice sheet in Ross Embayment. (I) Inferred stages and events in the development of the AIS across the E-O boundary and the relationship to orbital forcing are summarized.

**Fig. 3.** Major glacial events (grey bands) recorded by clast abundance peaks from the CRP-3 core (A) calibrated to the astrochronologically-tuned  $\delta^{18}\text{O}$  record from ODP Site1218 (3) (B). Major peaks in clast abundance from CRP-3 correspond to the onset of the EOT-1 shift, and glacial maxima at the Oi1 and Oi1a, and are associated with prolonged intervals characterized by cold southern high latitude summers as expressed in the 70°S mean summer insolation (C). AIS volume changes recorded by the sedimentary sequences and clast abundance (see Fig. 2) are paced by the influence of obliquity and precession on a smaller-sized terrestrial ice-sheet (D) between 34.2-32.8 Ma. Comparison with available atmospheric  $p\text{CO}_2$  records based on Boron-isotope (2) and Alkenone (7) proxies (E) shows that the first evidence of ice sheet grounding in the CRP-3 core and a major peak in clast abundance occurs at the Oi1a event (32.9-32.8 Ma), and coincides with a longer-term drop in atmospheric  $\text{CO}_2$  drop to below ~600 ppm.

### Supplementary Materials:

Materials and Methods

#### *The CRP-3 Core Stratigraphy & Interpretation of Sedimentary Cycles*

Drilling at CRP-3, ~12 km east of Cape Roberts provided an almost continuous core through 823 m of Cenozoic sedimentary strata on the western edge of the Victoria Land Basin (VLB), at the Western margin of the Ross Sea continental shelf (31). At 823 metres below the sea floor (mbsf) the basement of the VLB was penetrated and a further 133 m of basement rocks was recovered and correlated with the Devonian-age, Arena Sandstone of the Beacon Supergroup.

The CRP-3 succession contains an array of lithofacies comprising fine-grained mudrocks, interlaminated and interbedded mudrocks/sandstones, mud-rich and mud-poor sandstones, conglomerates and diamictites that are together interpreted as the products of shallow marine to possibly non-marine environments of deposition, affected by the periodic advance and retreat of a land-terminating and tidewater glacier (14, 32) The uppermost 330 metres below sea floor (mbsf) show a cyclical arrangement of lithofacies similar to those recognised throughout CRP-2/2A drill core (14, 15), and are interpreted to reflect cyclical variations in relative sea level in concert with variations in the proximity of a marine-terminating glacier, ultimately regulated by fluctuations in the volume of the AIS (15). Sedimentary cycles of this type were termed “Motif A” cycles or depositional sequences in Ref. (14), but are referred to here as “Type A” sequences (Fig. S1).

Between 330 and 780 mbsf, cyclical units generally characterised by fining-upward successions from conglomerate above a sharp boundary passing into sandstone facies, have been identified as “Type B” (15) (Fig. S1). Sedimentary cycles of this type were termed “Motif B” cycles or

depositional sequences in Ref. (14), but are referred to here as “Type B” sequences.

These Type B cycles were interpreted as fluvial to shallow-marine deltaic depositional sequences recording cyclical variations of relative sea-level in concert with a more “indirect” record of the proximity of an advancing and retreating land-terminating ice margin. A total of thirty-seven Type B sedimentary cycles, occur below 300 mbsf (15, 17), and are associated with <20 m oscillations in relative sea-level on the following basis. The sandstone intervals of Type B cycles are composed of poorly-sorted sandstone (Facies 3) and well-sorted stratified sandstone (Facies 4/5). Facies 4/5 dominates the upper parts of these cycles and contains hummocky cross-stratification, low angle cross stratified intervals, symmetrical (wave-induced) ripples, shallow-marine bioturbation (*skolithos* to *cruziana* ichnofacies) and marine molluscs consistent with a wave-influenced inner shelf to shoreface above storm wave-base, with decreasing glacial influence. Underlying this is Facies 3 which contains evidence of sediment gravity flows in a shallow marine depositional setting; possibly a marine delta that is more proximal to the shoreline being feed by a fluvial system debouching from a land-based glacier terminus. At the base of each sequence are poorly sorted conglomerates of possible fluvial, but most commonly of marine affinity, interpreted as the most proximal to a land-terminating glacier and associated fluvio-marine deltaic system.

At about 300 mbsf the first diamictites occur recording the development of a more expansive marine-terminating ice sheet on the western Ross Sea continental shelf for the first time. Above this level, eleven Type A glaciomarine sedimentary cycles associated with larger sea-level fluctuations of >20 m are bounded by glacial surfaces of erosion, which implies the loss of part of the sedimentary record (14). Water depth changes in Type 2 cycles represent oscillations between innermost shelf (~5m) and the offshore low energy shelf below wave base (up to ~50m) (33). The coarse grained basal units of Type A cycles comprise massive and/or interstratified diamictite and/or poorly sorted conglomerates (Facies 6/7/9/10) overlying a sharp unconformable surfaces representing glacial overriding environments proximal to the grounding line. Underlying facies are deformed displaying clastic intrusions, intraclast and physical intermixing of lithologies. The overlying diamictite and conglomerate facies are consistent with a combination of glaciomarine processes, including subglacial deposition and deformation, melt-out and rain out of debris during ice withdrawal, and pro-glacial debris flow deposition with ice berg rafting during retreat of the marine grounding line. Above basal coarse grained facies are rhythmically stratified units (Facies 8) that are the product of suspension deposition from turbid plumes associated with subglacial streams discharging near marine grounding line fans. The upper portions of this fining-upwards facies succession comprise a sparsely fossiliferous and bioturbated sandy mudstone and mudstone (Facies 1/2) corresponding to a zone of maximum water depth, the glacial minimum, and lowest sedimentation rate in the cycle. This unit then passes up gradationally into an interval of poorly-sorted bioturbated muddy-sandstone with increased evidence of ice berg rafting (Facies 3), which in turn grades upwards (when preserved below the next glacial surface of erosion) into moderately to well-sorted stratified fine sandstone of inner shelf to shoreface affinity (Facies 4/5). The drilled strata accumulated in the Victoria Land Basin some tens of kilometers seaward of the present day coast. Accommodation space for the preservation of such a remarkably complete sedimentary record, was provided by high rates of tectonic subsidence during the initial stages of rift extension beginning in the latest Eocene (34, 35).

### *Paleogeographic and Tectonic Setting of the CRP 3 Core*

Uplift of the Transantarctic Mountains (TAM) began about 45Ma (based on fission track thermochronology e.g. (36) as rift shoulder uplift at the margin of the evolving West Antarctic Rift System (WARS), and by 34Ma was a significant source of sediment to the Western Ross Sea margin of the Victoria Land Basin (VLB). Seismic stratigraphy and geological history for the VLB (35) shows that rapid syn-rift subsidence did not occur in McMurdo Sound/Southern Victoria Land until around 35 Ma and the CRP3 sequences (Type B) were deposited in fluvio-marine fan deltas on the steep margin of the TAMs, which during the Late Eocene likely supported a mountain ice cap/ice sheet, e.g. (1). It was a cooling climate, driven by CO<sub>2</sub> decline during this time that initiated continental scale glaciation which involved ice overriding and down cutting in the TAM as the EAIS expanded forming the McKay and other outlet outlet glaciers.

### *Luminance record*

The luminance record has been obtained from image analysis of digital photographs using the freely distributed ImageJ software of NIH. The luminance record reflects fluctuations in the abundance of two sedimentary end members (i.e. clay and sand) of different grain-size, which following the interpretation of sedimentary environment (15-16, 37) reflect oscillations in depositional energy, themselves controlled by the combination of changes in water depth and glacial proximity. With the limits imposed by the fact that the luminance record does not actually record grain-size changes within different classes of sedimentary components, but only their relative abundances, our record represents an approximation of cycles of advance and retreat of the ice-sheet and related changes in the sedimentary environment.

### *Significance of Clast Lithologies*

Distribution patterns and petrographical, mineral and chemical analyses allowed several categories of clasts to be distinguished throughout the CRP-3 succession (30), which are derived from the erosion of the different rock types exposed on the Transantarctic Mountains (TAM). Importantly, the presence of lithologies derived from the lower levels in the TAM rock succession exposed along the Mackay valley in the lower half of CRP-3 core (30) suggests that the Mackay valley was already present during the deposition of the CRP-3 succession, implying a direct connection with the interior Antarctic Ice Sheet (AIS).

### *Cyclostratigraphic Analysis*

Lithological changes and stratigraphic sequences from the Oligocene CRP record reflect ice volume changes that have been linked with orbitally driven climatic cycles (15, 16) and thus provide an opportunity to directly compare the record of proximal ice volume changes with available high-resolution temperature and ice-volume proxy records derived from oceanic sequences. Hence, the first goal of our cyclostratigraphic analysis is to test the presence of periodic components in the alternations of conglomerates/diamictites and fine- to coarse-grained sandstone in the Type A cycles from the upper interval of the core above 330 mbsf. We use



previously published cyclostratigraphic results (17) for the Type B cycle interval (below 330 mbsf). Given the large difference of facies arrangement, sequence architecture and sedimentation rate (14), cyclostratigraphic analysis has been performed separately on Type A and Type B stratigraphic intervals.

To establish a basic framework for the cyclostratigraphic interpretation of the lower Oligocene at CRP-3 (i.e. the upper 330 meters), we applied a Singular Spectrum Analysis (SSA) on the luminance and clasts records in the depth domain. SSA is a particularly well-suited method to analyse a complex system showing non-linear oscillations on multiple timescales, like the climate system (38). The purpose of SSA was to isolate from a large background red-noise, statistically significant oscillations in clast abundance and luminance, which are likely to represent the response to orbitally driven climate variations. Since these variations are expected to be harmonic, we especially focused on harmonic SSA-isolated components. In this case we use SSA because of the many (non linear) factors typically controlling different sedimentary components in a marginal, shallow-water depositional settings as that inferred for the CRP-3 glaciomarine sediments (39).

SSA was performed using the kSpectra Toolkit by SpectraWorks. The datasets were interpolated to an evenly spaced depth interval of 0.5 m and 1 m for luminance and clasts, respectively. We used an embedding dimension of 100 and 50 for luminance and clasts datasets, respectively, corresponding to about 1/6 of the dataset length.

The statistical significance of the SSA eigenvalues was evaluated using the Monte Carlo method (40). The eigenvalues spectrum, i.e., the eigenvalues plotted versus the main frequency of the corresponding Empirical Orthogonal Function (EOF) of the luminance dataset, is shown in Fig. S2c. The statistically significant EOFs 9, 10 and 16, 17 are shown in Fig. S2a and S2b. These two couples of EOFs, which exceed the upper significance level of 97.5%, represent in total ~9% of the total signal variability and have the characteristics of harmonic components. Other statistically significant EOFs, representing less than 1% of the signal variability, have been excluded.

Similarly to results obtained with the spectral analysis of the luminance record, the SSA spectrum of the interpolated clast abundance dataset (Fig. S3) shows one couple of eigenvalues (i.e. 6 and 7) with identical frequencies and exceeding the upper confidence limit. Although other marginally significant eigenvalues exist, EOFs 6 and 7 again represent harmonic components of the clast signal (Fig. S3b), and therefore, were used to reconstruct the filtered clast signal. EOFs 6 and 7 represent ~10% of the total clast abundance record variability. A spectral analysis of the unevenly spaced clast abundance record carried out with the Lomb-Scargle method reveals significant spectral densities at the same frequency as the SSA (Fig. S4).

Power spectrum density of the SSA-reconstructed signals (Fig. S5a and S5b), computed with the Blackman-Tukey method (Fig. S5c), shows that the harmonic components isolated by SSA (Fig. S5a, b) have well defined spectral peaks and their frequencies are proportional to that of Earth's axis inclination (clasts) and orbital precession (luminance), based on sedimentation rates calculated for the upper part of the CRP-3 core (13). Moreover, the SSA-filtered luminance shows a well-defined modulation that was reconstructed using a Hilbert transform. The “envelope” of SSA-filtered data has a main frequency that is proportional to that of short (~100kyr) orbital eccentricity. This provide robust evidence that the SSA-filtered oscillatory

components of the analysed dataset represent a direct effect of Earth's orbital variations on the sedimentary record. In our interpretation, the prevalence of the obliquity forcing on the clast abundance record result from the main advance and retreat of a larger Oligocene ice sheet, which is mostly controlled by Earth's axial inclination.

## Age Model

The magnetostratigraphic analysis of the CRP-3 drill hole allowed identification of a normal polarity interval ascribed to magnetochron C13n between 340 - 627 mbsf (13). In spite of the lack of standard biostratigraphic events in the lower part of the core, the lack of the Transantarctic Flora, whose maximum age corresponds to Chron C15n, suggests a maximum Late Eocene (~35 Ma) age for the bottom CRP-3 core (41).

However the magnetostratigraphic interpretation of the lower part of the core was based on poor magnetic properties for some intervals (41). Accordingly, the reliability of the magnetostratigraphic record from the lower part (below 300 mbsf) of the CRP-3 has been recently questioned (17). Cycle counting indicates a ~900 kyr duration for Chron C13n as originally described (13), which is much larger than the ~548 kyr duration estimated on the basis of cyclochronology (24). This mismatch can be ascribed to the poor paleomagnetic record for the lower part of the core due to a relatively low magnetic intensity in the interval between ~243 and 627 mbsf (41). In particular, the inclination record of the original magnetostratigraphic data (41) has mixed polarity between 359 and 370 mbsf with most of the fluctuations represented by single samples. These changes are mirrored by changes in *k* and NRM suggesting they are related to variations in diagenetic redox conditions. Between 370 and 440 mbsf, the paleomagnetic data are of particularly poor quality: there are only 8 samples out of a total of 91 analysed specimens that gave interpretable magnetostratigraphic results (Fig. S6). These sparse 8 samples were originally interpreted as of normal polarity but with the new interpretation provided by (17), these 8 samples should be considered remagnetized and we retain the interpretation of Florindo et al. (13) only for the interval below 440 mbsf. The expected position of C13n based on cyclochronology and comparison with the available astrochronology (3, 24) is reported in Figure S7.

Cycle counting throughout the Type B interval allows calibration of glacial phases identified by major clast peaks to the astrochronologically dated isotope record of the equatorial Site 1218, under the assumption that the dominant periodicities observed in the clast record reflect obliquity forcing (17). Here we complement this approach by counting cycles identified in the SSA-reconstructed clast and luminance component throughout the Type A interval. We use the C12n/C12r Chron boundary at 16.7 mbsf (13), dated at 31.3 Ma (3, 24) as an absolute age starting point for cycle counting.

Based on available bio- and magneto-stratigraphic chronology and radiometric dating (13), the best fit sedimentation rate within the uppermost 150 m of the CRP-3 core is ~150 m/Myr. Counting of precession (SSA-filtered luminance), obliquity (SSA-filtered clasts) and short eccentricity (envelope of luminance) cycles allows quantifying the stratigraphic gaps at the top each sequence (Fig. S8). The stratigraphic position of glacial maximum intervals (grey bands) correlates with positive shifts in the  $\delta^{18}\text{O}$  record using the astrochronological age of magnetochron C12r/C12n boundary (31.05 Ma) as a time constraint. Remarkably the astrochronological age obtained for the first diamictite deposits occurring at 330 mbsf based on

cycle counting of the upper part of the core, coincides with the age obtained by Galeotti et al. (17) based on cycle counting from the bottom of C13n.

### Glacial Isostatic Adjustment (GIA) modeling

The recorded relative sea level (rsl) fluctuations show that during (local) glacial maxima, the CRP-3 site is characterized by rsl lowstands. Conversely, local rsl highstands occur throughout ice-free conditions. Therefore, the observed local rsl change is in phase with the eustatic trend. However, given the proximity of the CRP-3 drill site to the AIS margins, it is expected that the ice-driven perturbations of the gravitational pull combined with the crustal deformations would result in local rsl changes that are opposite in sign to the eustatic signal and likely of larger amplitude (as described by the GIA theory).

Therefore we argue that the CRP-3 drill site is located at a very peculiar position with respect to the evolving East and West ice-sheets and that the GIA deformations induced by EAIS and WAIS might balance each other and result in a local rsl curve that is in phase with the eustatic trend. This implies a peculiar behavior of the WAIS and EAIS that is likely to be related to hysteresis.

To test this hypothesis we have performed numerical GIA simulations according to three simple models for the spatio-temporal variation of the AIS thickness that follow the same 540 kyr-long ice-volume chronology (Fig. S9). Our predicted scenarios are not intended to precisely reconstruct the chronological succession of events that characterized the AIS and rsl fluctuations across the whole EOT. Rather, our simulations provide likely rsl responses of the CRP-3 drill core site to plausible AIS fluctuations.

We solve the gravitationally self-consistent Sea Level Equation by means of the pseudo-spectral method (42). We employ a spherically symmetric, radially stratified, self-gravitating, rotating, deformable and incompressible Earth model (42). We assume a 100 km thick elastic lithosphere and a three-layer Maxwell viscoelastic mantle characterized by an Upper Mantle (UM), a Transition Zone (TZ) and Lower Mantle (LM). We choose a UM viscosity of  $0.25 \times 10^{21}$  Pa·s, a TZ viscosity of  $0.5 \times 10^{21}$  Pa·s and a LM viscosity of  $1.0 \times 10^{22}$  Pa·s. The core is assumed to be inviscid.

We employ the global topography/bathymetry from (43) where the Antarctic continent is described by Wilson et al. (10) maximum topography.

We consider three different models for the spatio-temporal ice-thickness variation that follow the same AIS volume fluctuation of Fig. S9

1. AIS-1. We use the fully grown AIS as from Stocchi et al. (44) and uniformly scale the ice thickness to obtain an initial AIS volume of 30 m esl. Then, we impose that the AIS volume follows the curve of Fig. S9 (see Fig. S10). The latter is characterized by an initial 40 kyr cycle during which the AIS gains 10 m (esl) and then returns to its initial volume. Then, a 100 kyr-long cycle follows with a 20 m esl AIS fluctuation. Afterwards, a final 400 kyr cycle occurs during AIS reaches 70 m (esl) before returning to its initial volume. Accordingly, we linearly scale the ice thickness in time and solve the SLE to compute the rsl change at CRP-3 site. The resulting rsl curve (blue) is always in anti-phase with respect to the eustatic (Fig. S11). This follows from the proximity of grounded ice nearby the CRP-3 site throughout the entire chronology. The modeled rsl curve,

therefore, does not agree with the inferred rsl variation as recorded by the CRP-3 sediment core

2. AIS-2. We keep the same AIS volume chronology from the previous case but allow for a realistic spatial variation of ice thickness according to the EOT AIS model from Stocchi et al. (44). Therefore, the AIS growth occurs heterogeneously in space as a function of ice-flow dynamics (Fig. S12). Accordingly, the predicted rsl curve follows the eustatic but is characterized by larger fluctuations (larger rsl drops) because the CRP-3 site sits on top of the peripheral forebulge. The latter is uplifted by the thickening AIS and then subsides during the interglacials. However at ~200 kyr (model run time) the predicted rsl drop that accompanies the AIS growth stops and, after ~60 kyr of almost stable rsl, is followed by a ~40 m rsl rise. The latter stems from the GIA-induced perturbations that are related to the grounding of ice in the proximity of the CRP-3 site. Such a strong deviation from the eustatic trend during the AIS expansion is not observed throughout the CRP-3 record.
3. AIS-3. We perform a linear interpolation between the glacial minima and maxima from the previous model. The resulting rsl curve is in phase with the eustatic trend throughout the whole chronology and is also similar to the previous case until 140 kyr (model run time). Afterwards, in fact, the ~60m rsl drop that is caused by the uplift of the peripheral forebulge (previous case) is counteracted by the synchronous ice-sheet thickening on West Antarctica and by the ice-sheet grounding on the Ross Sea. Regardless of the actual amplitude of the predicted rsl change, this simulation is in agreement with the inferred rsl change that is based on the CRP-3 core. Accordingly, we argue that WAIS expansion and grounding on the Ross Sea occurred (almost) synchronously with the EAIS thickening. The latter, in fact, results in a larger than eustatic rsl drop in the Ross Sea and this creates space for WAIS to grow. The grounding of WAIS results in a rsl rise that counteracts the rsl drop from EAIS thickening. As a result, the CRP-3 drill site experienced a nearly eustatic rsl trend despite its proximity to the AIS margins.

**Fig. S1.** Diagram showing the character of sequences in the CRP3 drillhole and their interpretation; from (14). (A) fully-developed sequence Type “A”, (B) less fully developed/cryptic Type “B”. SB/GSE – Sequence Boundary/Glacial Surface of Erosion, SB/RS – Sequence boundary amalgamated with transgressive Ravinement Surface, TS – Transgressive Surface, MFS – Maximum Flooding Surface, RSE – Regressive Surface of Erosion, LST– Lowstand Systems Tract, TST– Transgressive systems Tract, HST– highstand Systems Tract, RST – Regressive systems Tract. Facies codes are explained in text.

**Fig. S2.** SSA Eigenspectrum (A) and statistically significant (>97.5%) EOFs (B, C) according to a red noise Monte Carlo Test of the luminance record.

**Fig. S3.** SSA Eigenspectrum (A) and statistically significant (>97.5%) EOFs (B) according to a red noise Monte Carlo Test of the clast abundance record.

**Fig. S4.** Lomb-Scargle periodogram of the unenvly spaced record of clast abundance.

**Fig. S5.** Time series of the CRP-3 clast (A) and luminance (B) records filtered by Singular Spectrum Analysis (SSA) throughout the base of sequence 1 and the more complete (14-16)

sequence 2 (16.72-95.48 mbsf) and sequence 3 (95.48-157.22 mbsf). (C) Blackman-Tukey spectral analysis of the SSA-filtered clast (blue) and luminance (green) time series. The Blackman-Tukey spectral analysis of the envelope (red line in panel **B**) of the SSA-filtered luminance record is also reported. Note how the ratios between the periodicities coincide with those for precession (SSA-filtered luminance), obliquity (SSA-filtered clasts) and short eccentricity (envelope of luminance) periods. Vertical dashed lines represent the boundaries of sequences 2 and 3.

**Fig. S6.** Lithostratigraphic log of the CRP-3 drill-core and down-core variations of magnetic inclination.

**Fig. S7.** Calibration of the SSA-reconstructed obliquity component in the clast abundance from the lower part of the CRP-3 Core (depth domain) against the astrochronologically calibrated  $\delta^{18}\text{O}$  record of ODP Site 1218 (18).

**Fig. S8.** Calibration of the upper 300 m of the CRP-3 record to the Geomagnetic Polarity Time Scale and astronomical tuning to the La04 (21) orbital solutions. The calibration is based on counting precessional cycles identified in the luminance record and obliquity cycles identified in the clast abundance record (Fig. S2). Counting within individual stratigraphic sequences (14), allows estimating the gap implied by erosional surfaces across sequence boundaries.

**Fig. S9.** AIS volume fluctuation expressed in meters of equivalent sea-level (esl). An initial 40 kyr cycle is characterized by a 10 m esl fluctuation. Then, a 100 kyr-long cycle follows with a 20 m esl fluctuation. Finally a 400 kyr cycle occurs with a 40 m esl fluctuation. AIS volume during the interglacial is the same as the beginning.

**Fig. S10.** Snapshots of AIS-1 thickness during glacial minima, maxima and at intermediate stages.

**Fig. S11.** Predicted rsl curve (blue) according to the AIS-1 model. The proximity of CRP-3 site with respect to the AIS margins results in a rsl curve that is always opposite in sign to the eustatic curve (red). The amplitude of the predicted rsl curve is larger than the eustatic.

**Fig. S12.** Snapshots of AIS-2 thickness during glacial minima, maxima and at intermediate stages.

**Fig. S13.** Predicted rsl curve (black) according to the AIS-2 model. The predicted rsl curve is in phase with the eustatic but larger rsl drops characterize the first two cycles (the Ross sea is still ice free by this time) as a consequence of the uplift of the peripheral forebulge. An almost stable lowstand of about -65m characterizes the period between 200 and 280 kyr (model run time), when the EAIS component reaches its maximum size. Later a ~40 rsl rise accompanies the growth and grounding of WAIS on the Ross Sea and establishes a lowstand that is above the eustatic. Such a sudden change in the rsl trend is not observed in the data.

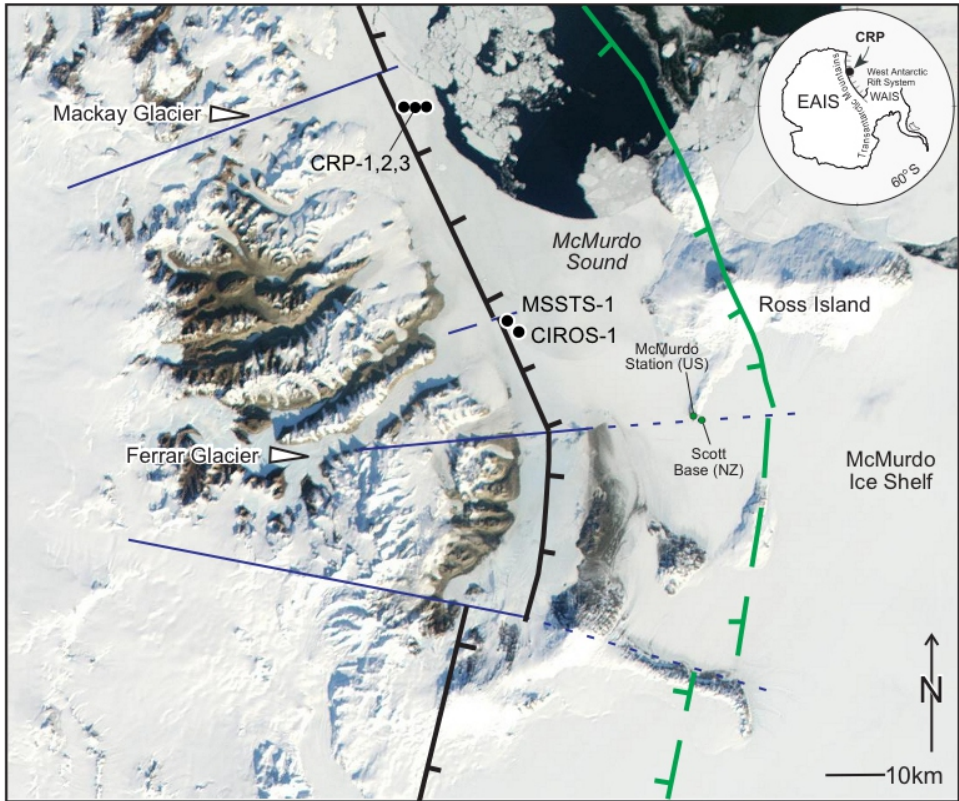
**Fig. S14.** Snapshots of AIS-2 thickness during glacial minima, maxima and at intermediate stages.

**Fig. S15.** Predicted rsl curve (green) according to the AIS-3 model. The predicted rsl curve is in phase with the eustatic throughout the whole chronology and is in agreement with the observed rsl fluctuations.

**Fig. S16.** A comparison of alkenone-based  $p\text{CO}_2$  composite from multiple marine sites as compiled in the study of Pagani et al. (7) and ODP Site 925 (23) for the time interval 38–24 Ma. Antarctic glaciation thresholds (approx. 750 ppm) deduced from climate models (1) is marked by a dashed line.  $\text{CO}_2$  estimates from Site 925 broadly agree with previously published composite alkenone– $p\text{CO}_2$  record for the Cenozoic. However, a systematic offset is apparent with Site 925 record indicating higher  $\text{CO}_2$  levels starting at ~32 Ma, compared to any other sites. According to Zhang et al. (23), this discrepancy can be attributed to regional differences in oceanography and algal growth environments, with Site 925 values capturing local conditions. For this reason we retain a value of ~600 ppm  $p\text{CO}_2$  from the multisite record (7) as the most likely threshold for AIS hysteresis.

#### References (31-44)

31. C. R. S. Team, *Terra Antarctica* **7**, 1 (2000).
32. R. D. Powell *et al.*, *Terra Antarctica* **8**, 207 (2001).
33. G. B. Dunbar, T. R. Naish, P. J. Barrett, C. R. Fielding, R. D. Powell, *Palaeogeogr. Palaeoclimatol. Palaeoecol* **260**, 50 (2008).
34. S. A. Henrys *et al.*, *Antarctica: A Keystone in a Changing World-Online Proceedings for the Tenth International Symposium on Antarctic Earth Sciences*, 4 (2007).
35. C. R. Fielding, J. Whittaker, S. A. Henrys, T. J. Wilson, T. R. Naish, - **260**, (2008).
36. P. G. Fitzgerald, E. Stump, *J. Geophys. Res. Solid Earth* **102**, 2156 (1997).
37. P. J. Barrett, *Terra Antarctica* **8**, 245 (2001).
38. M. Ghil *et al.*, *Reviews of Geophysics* **40**, 3 (2002).
39. C. R. S. Team, *Terra Antarctica* **8**, 1 (2001).
40. M. R. Allen, L. A. Smith, *Journal of Climate* **9**, 3373 (Dec, 1996).
41. F. Florindo, G. S. Wilson, A. P. Roberts, L. Sagnotti, K. L. Verosub, *Terra Antarctica* **8**, 599 (2001).
42. G. Spada, P. Stocchi, *Computers and Geosciences* **33**, 538 (2007).
43. M. Rugenstein, P. Stocchi, A. von der Heydt, H. Dijkstra, H. Brinkhuis, *Global and Planetary Change* **118**, 16 (2014).
44. P. Stocchi *et al.*, *Nature Geoscience* **6**, 380 (2013).



Alternate Fig. 1. Location of key geographical and tectonic features in southern McMurdo Sound, together with the location of the CRP, MSSTS-1 and CIROS-1 drill sites.

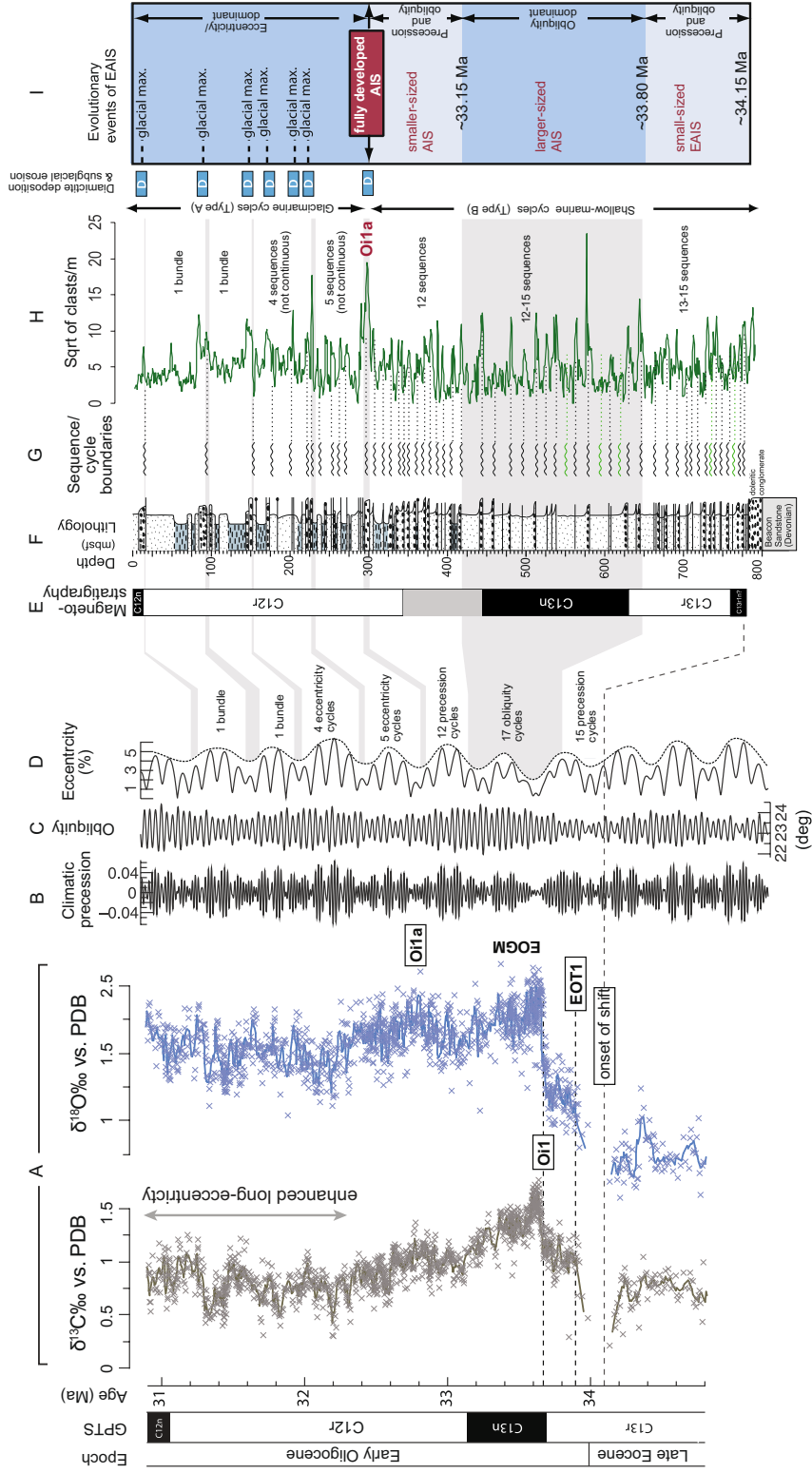


Figure 2



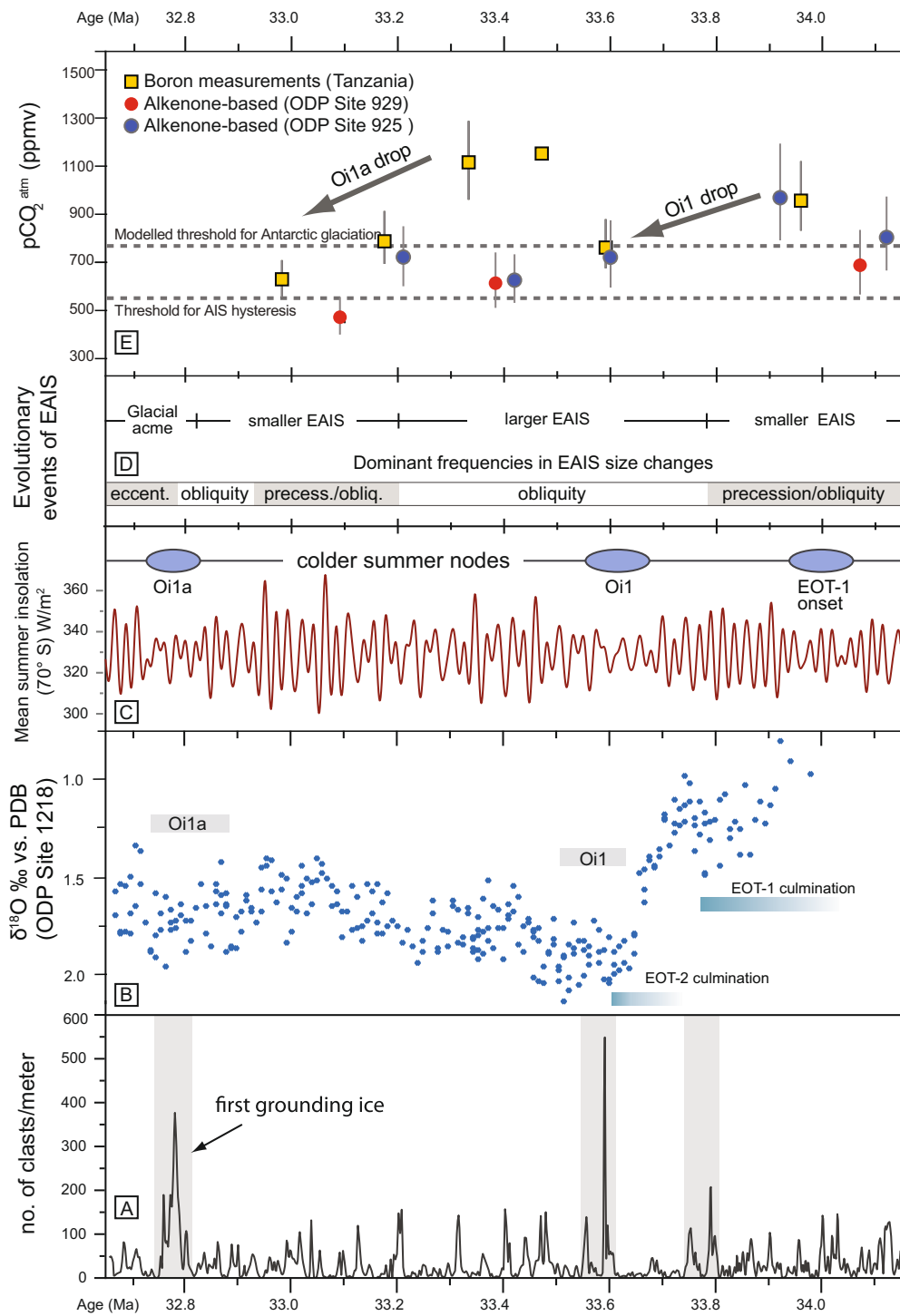
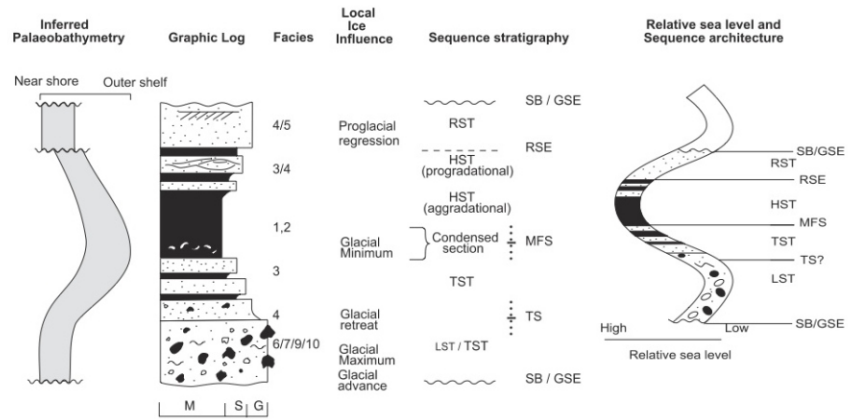


Figure 3

### IDEALIZED SEQUENCE TYPE A



### IDEALIZED SEQUENCE TYPE B

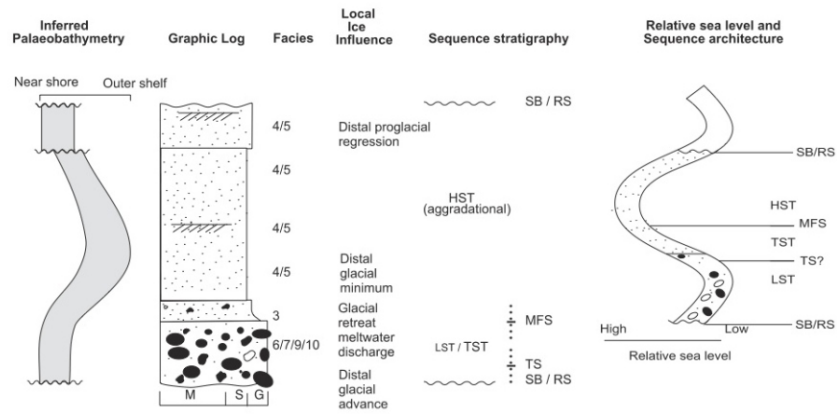


Figure S1

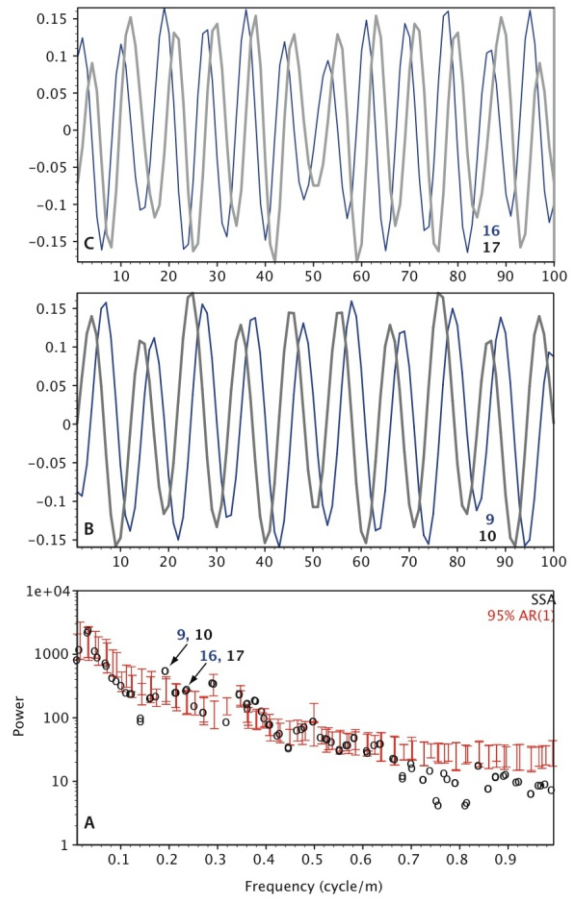


Figure S2

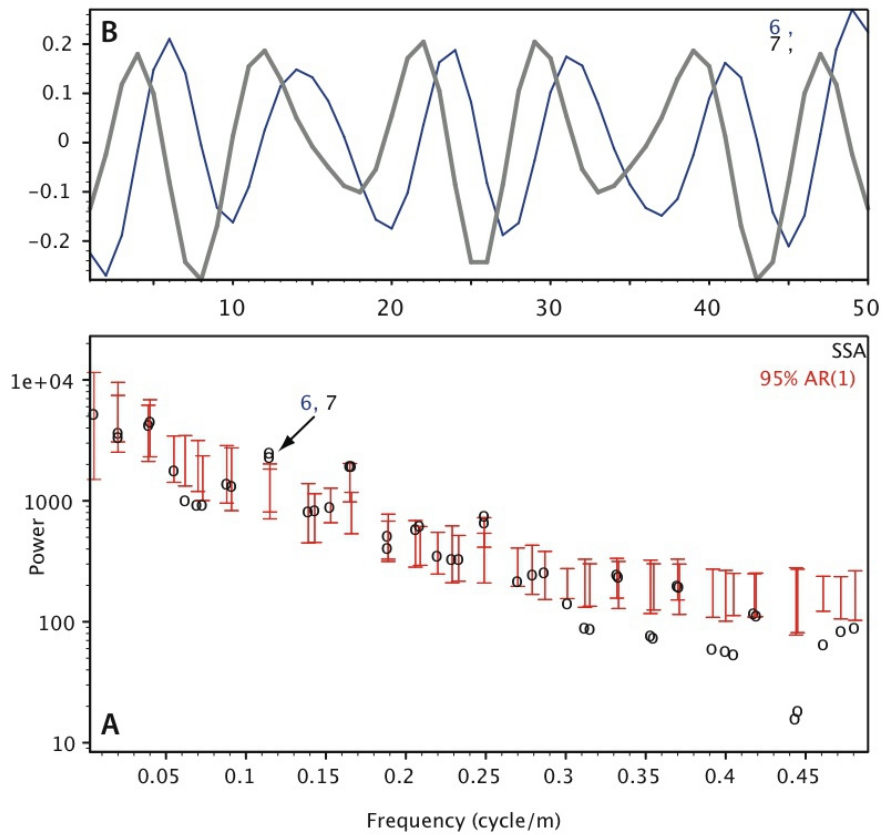


Figure S3

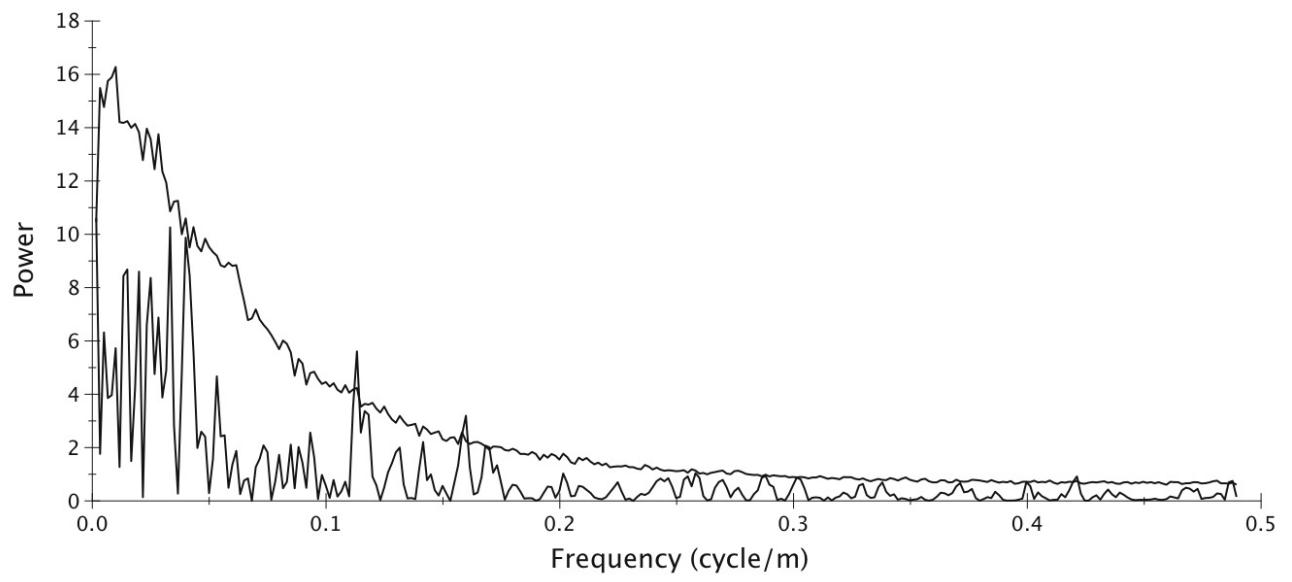


Figure S4

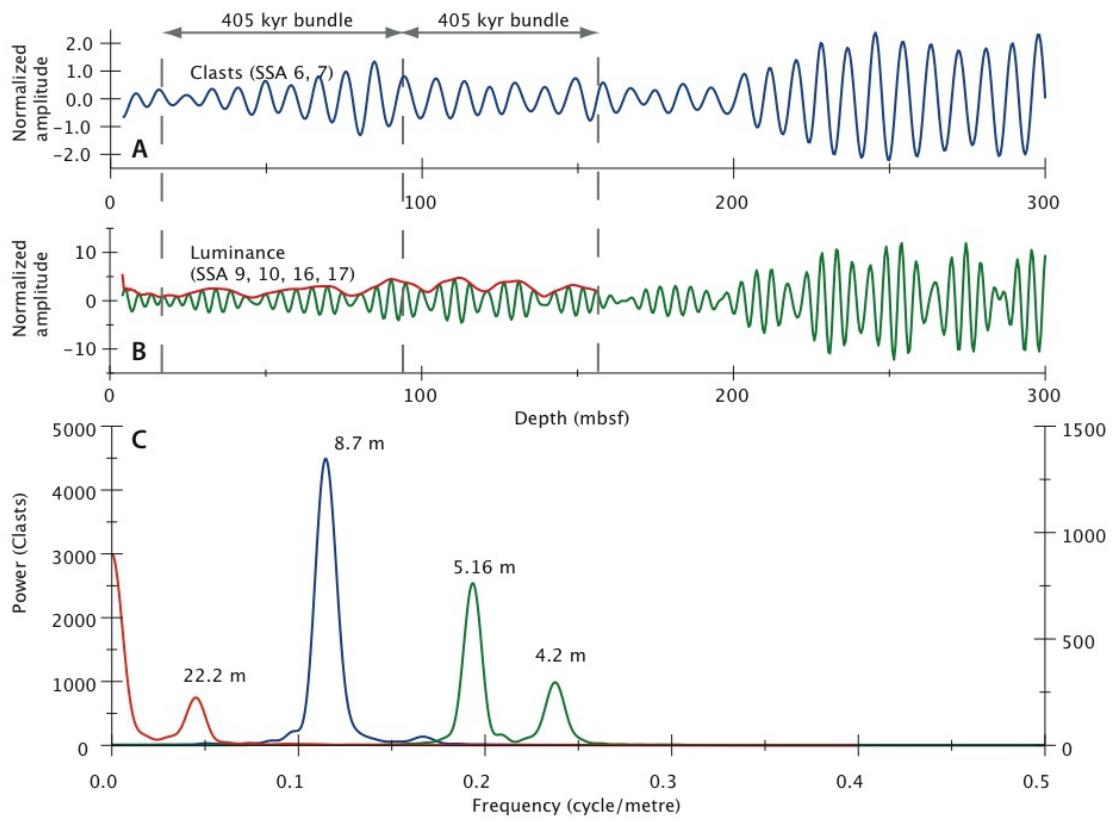


Figure S5

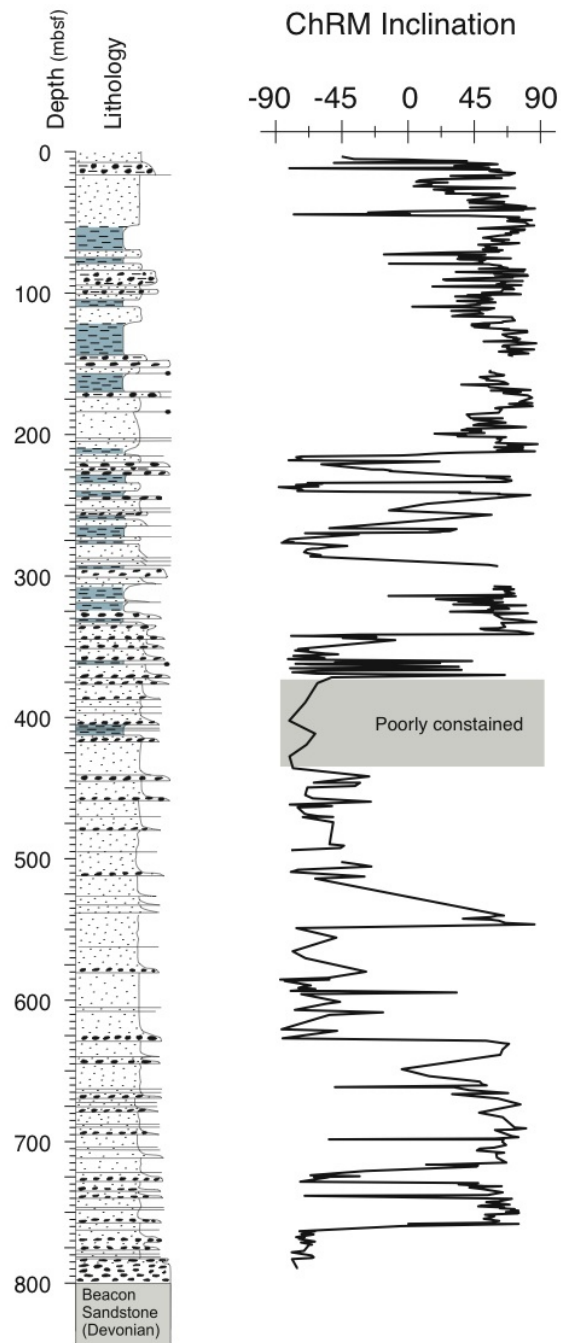


Figure S6

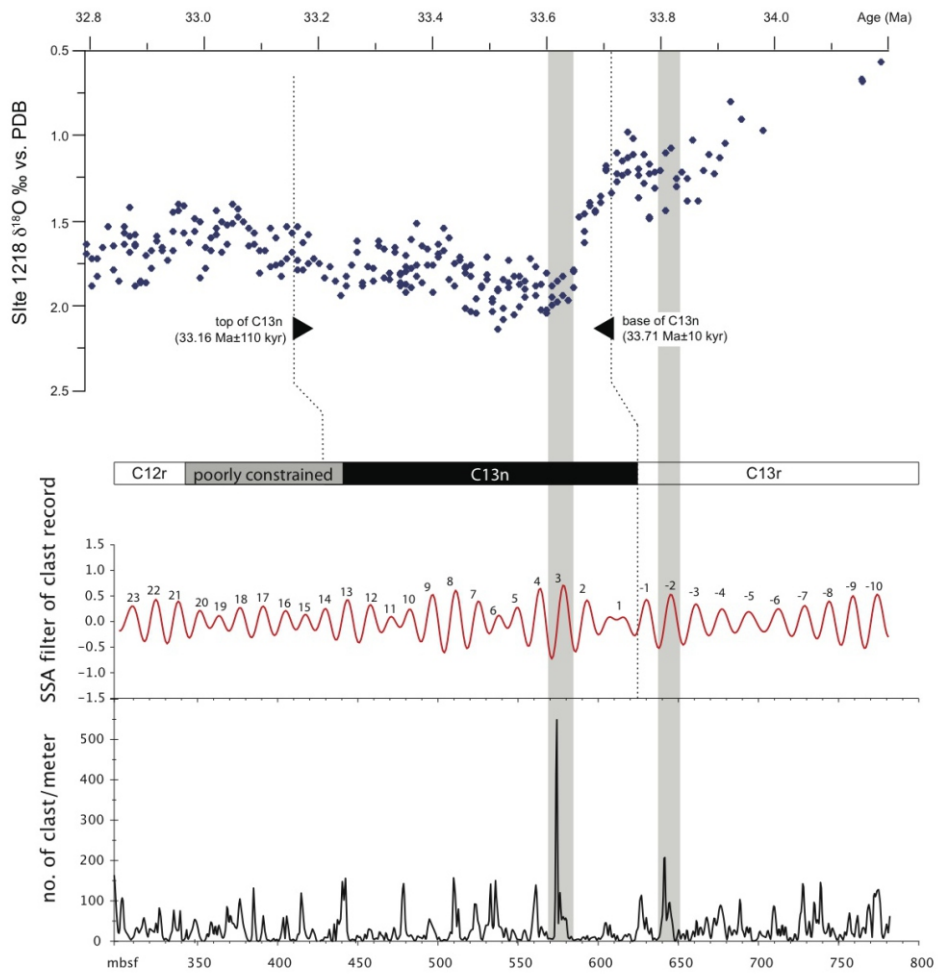


Figure S7



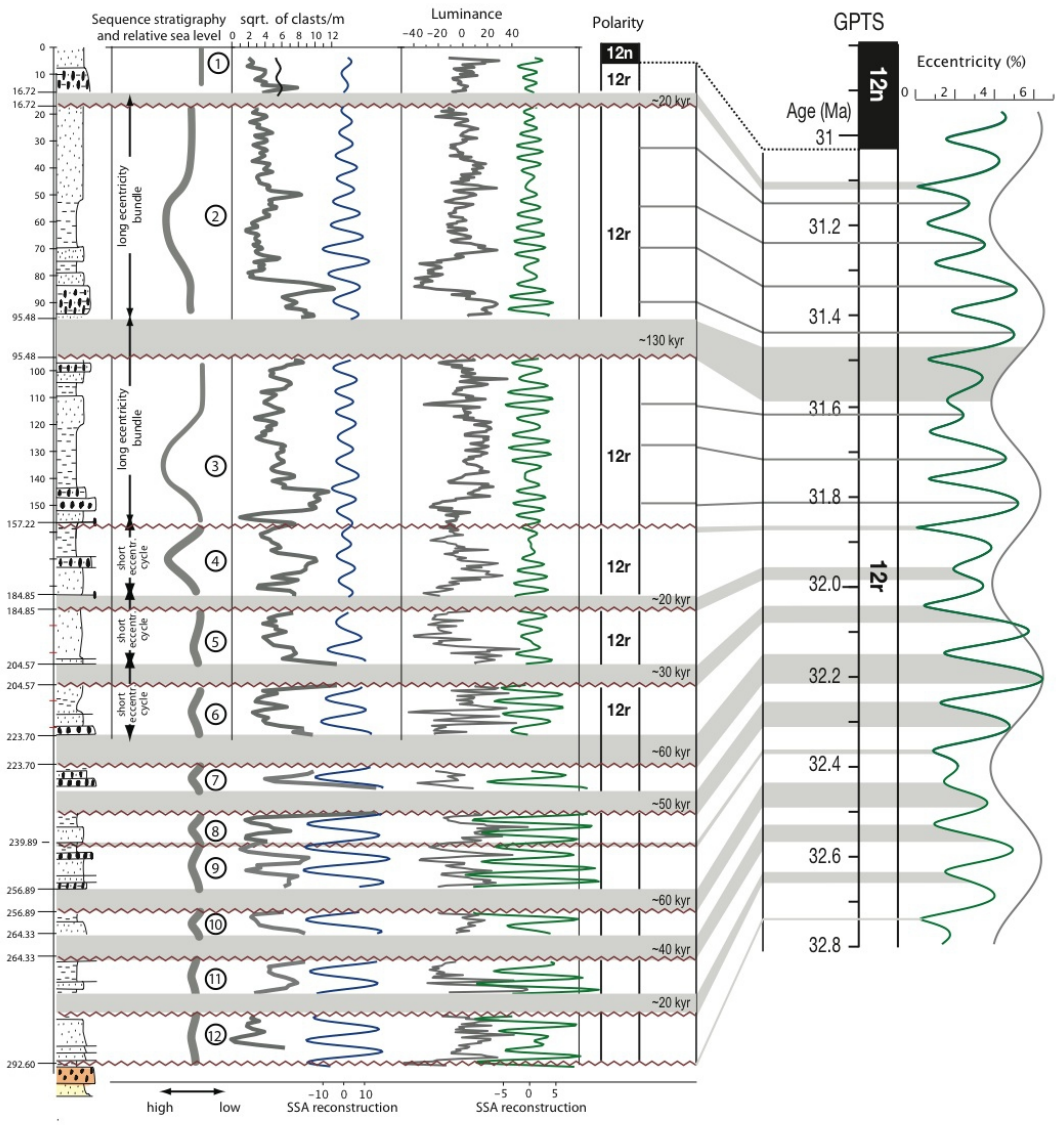


Figure S8

Figure S9

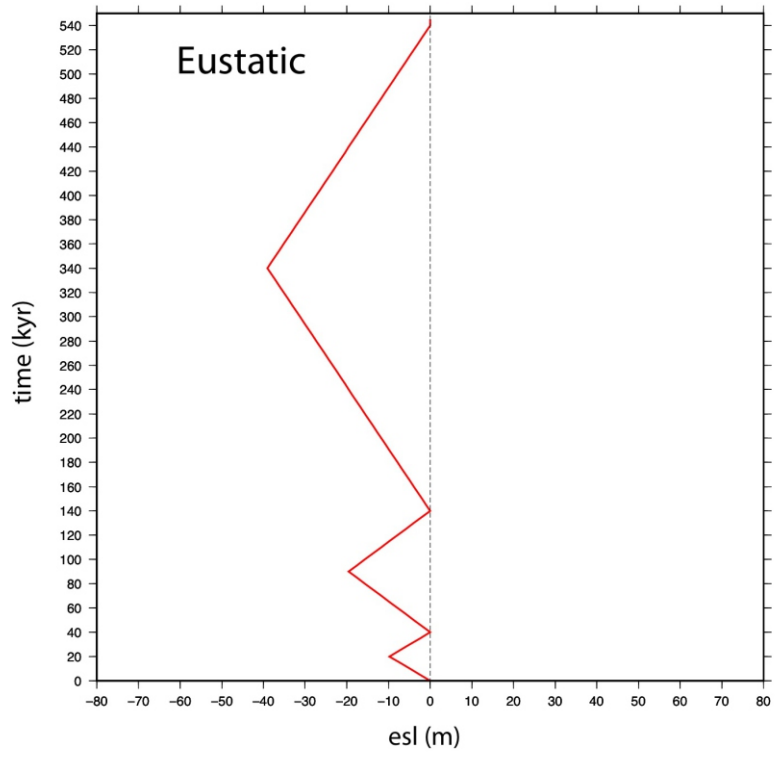


Figure S10

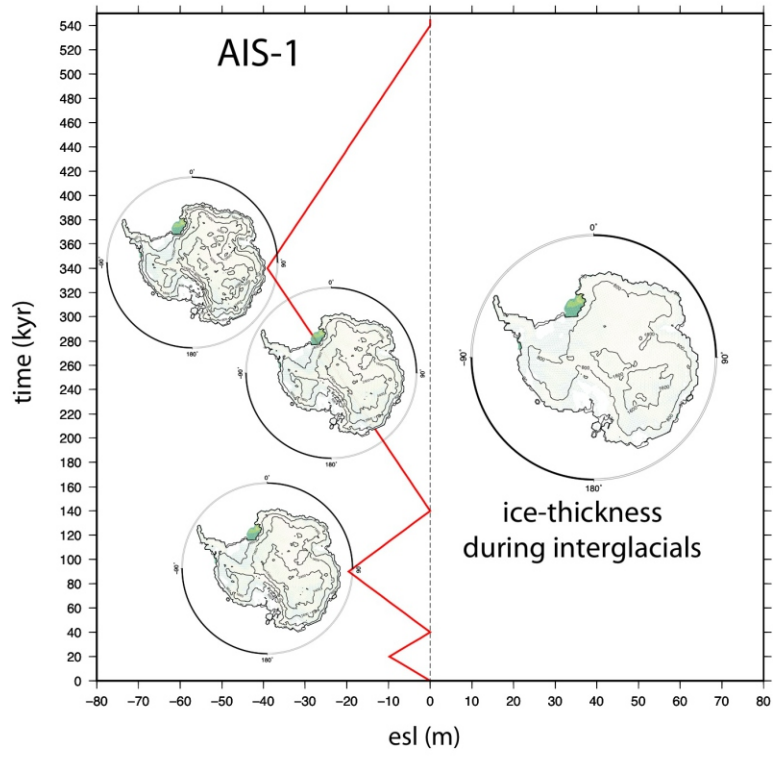


Figure S11

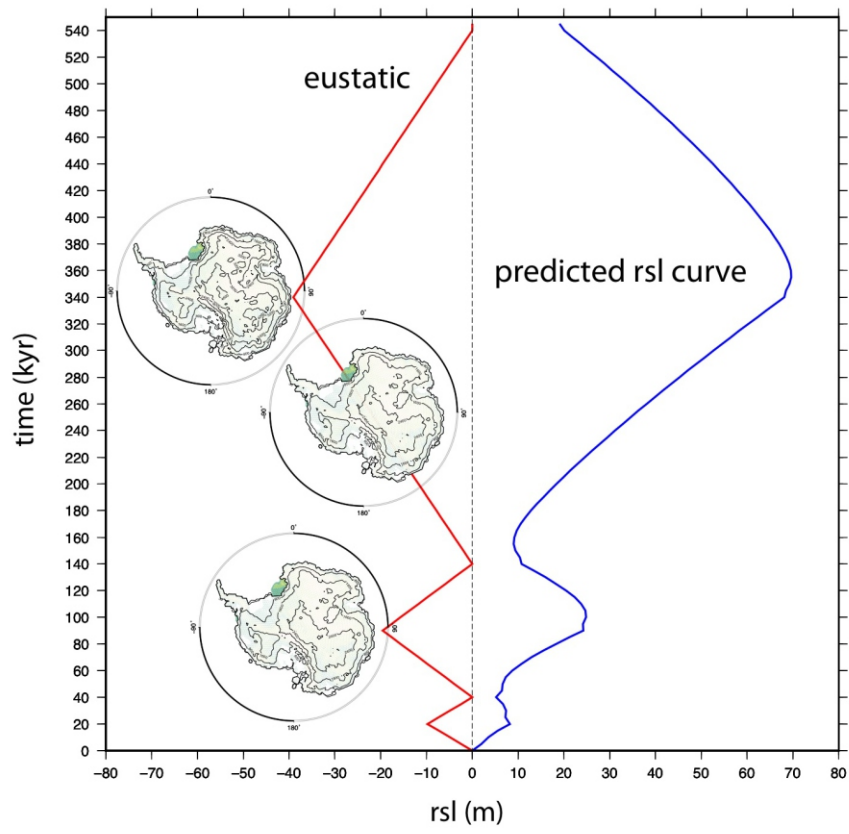


Figure S12

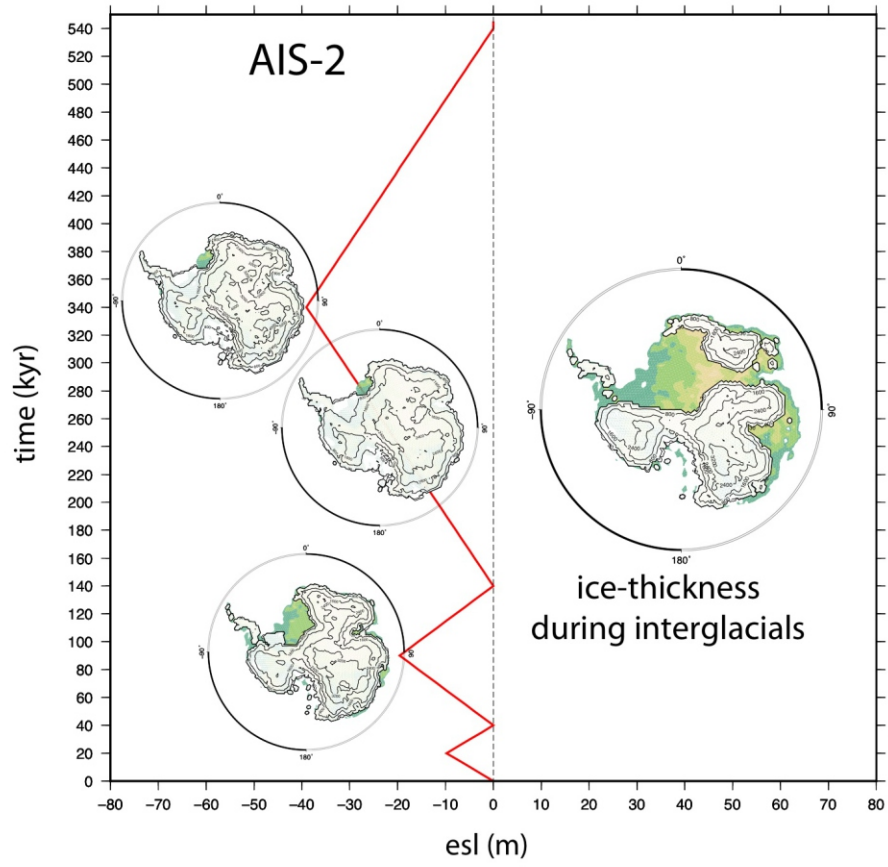


Figure S13

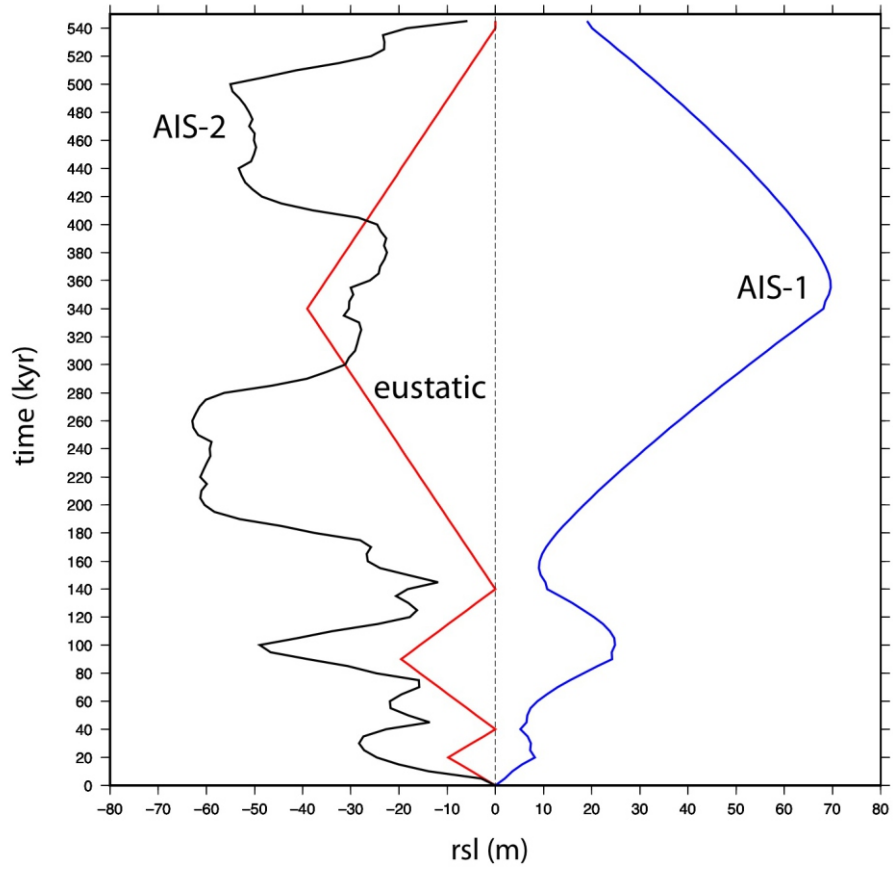


Figure S14

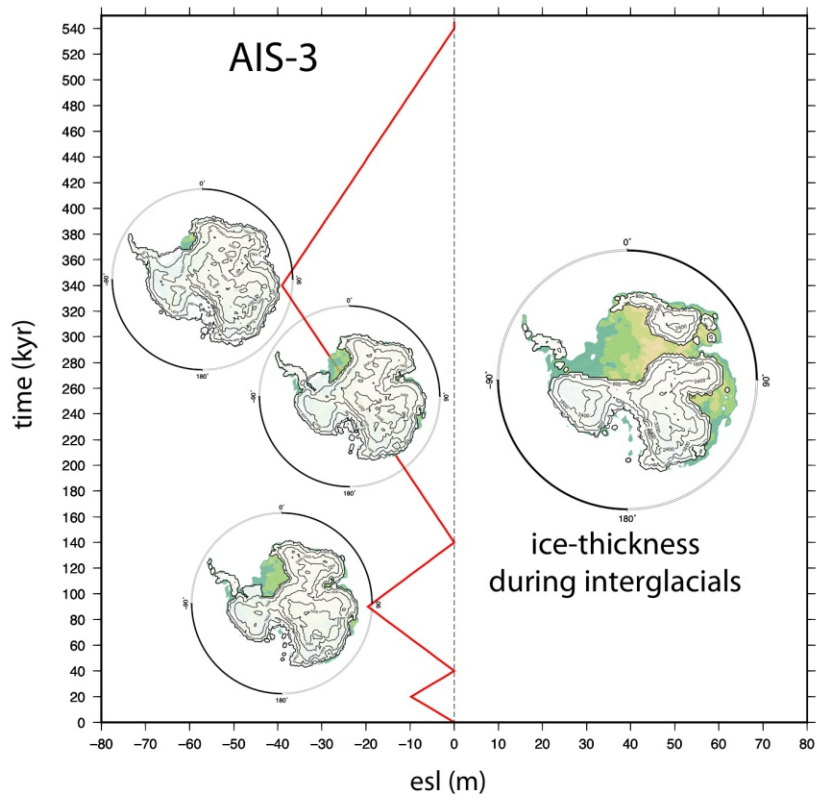
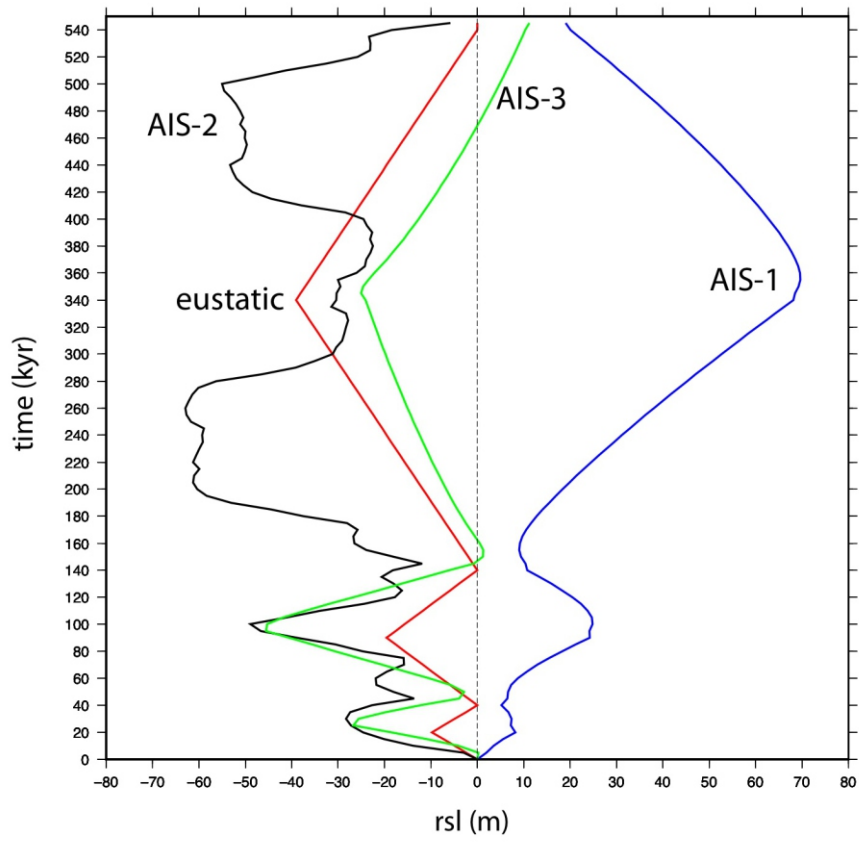


Figure S15





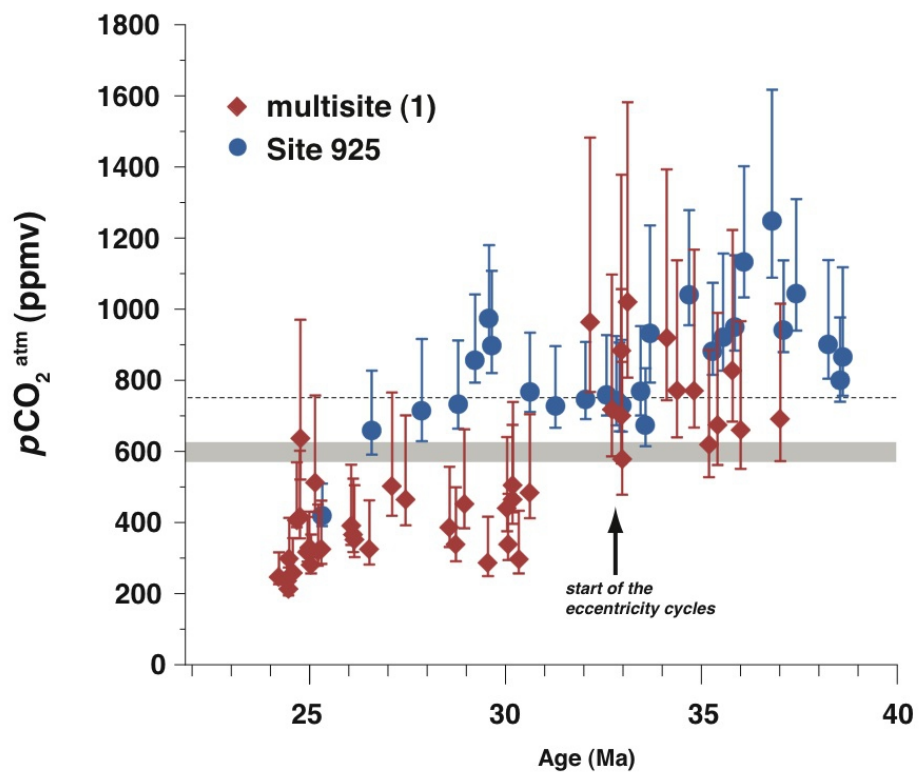


figure S16